Geophysical Journal International

Supplementary Material for "*Identification of two vibration regimes of underwater fibre optic cables by Distributed Acoustic Sensing*"

D. Mata Flores[1] , J.-P. Ampuero[1] , E. D. Mercerat[2] , D. Rivet[1] , A. Sladen[1]

[1] Université Cote d'Azur, CNRS, Observatoire de la Cote d'Azur, IRD, Géoazur, Sophia Antipolis, 250 rue Albert Einstein, 06560, Valbonne, France.

[2] CEREMA, Méditerranée, 500 Rte des Lucioles, 06560, Valbonne, France.

Contents of this file

Introduction

This supplementary contains additional figures and calculations.

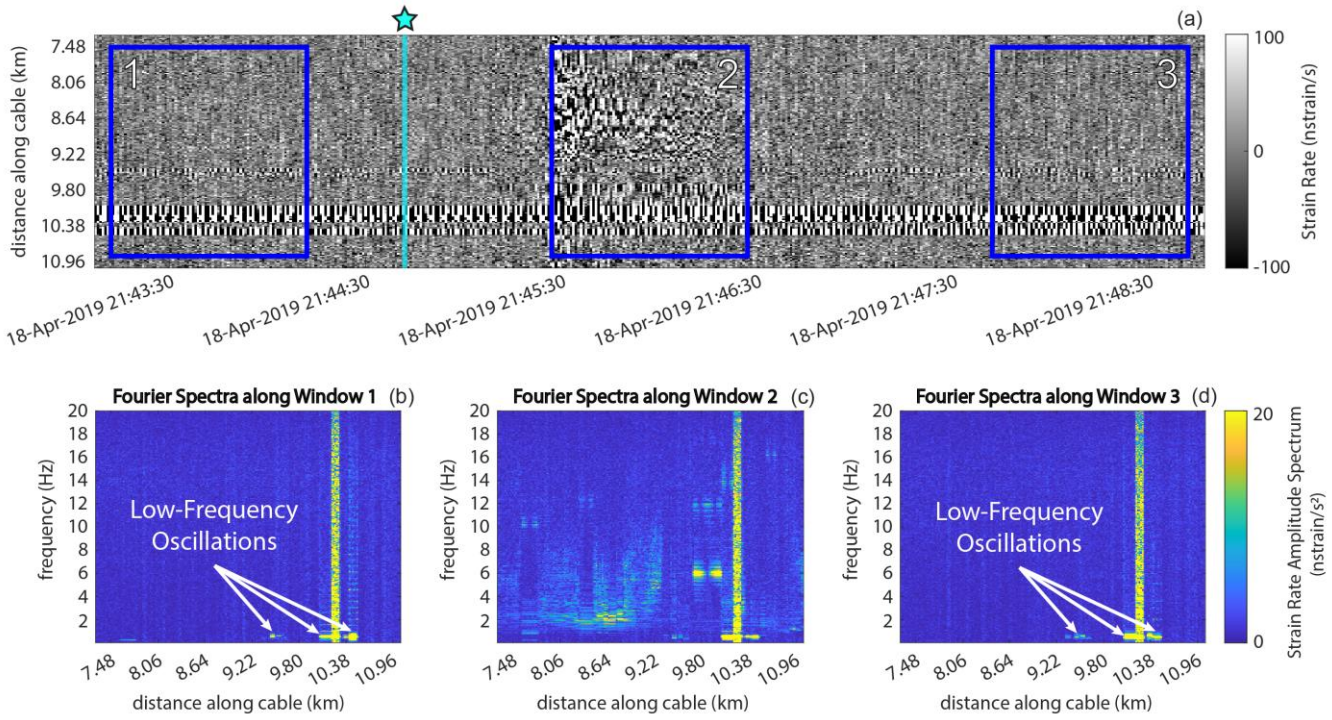

Supplementary Figure 1. High-frequency vibrations triggered along the HCMR fibre cable after a M_L-3.7 earthquake is recorded by DAS. (a) Low-pass filtered strain rate between km 7.48 and 10.96 along the HCMR cable, from 18-April-2019 21:43:07 to 21:48:47 UTC. Strain rate is filtered below 20 Hz. (cyan star) Origin time of the M_L-3.7 earthquake of Fig. 1 is indicated as reference. Waves trapped along certain cable sections can be observed in Window 2, after the arrival of seismic waves. (b), (c) and (d) Fourier Spectra between km 7.48 and 10.96 of a 1-min-long window starting: 90 s before the earthquake (1), 40 s after the earthquake (2) and 180 s after the earthquake (3), respectively. Fourier spectra before (b) and after (d) the earthquake are dominated by excited frequencies lower than 1 Hz. Fundamental-and-harmonic frequencies higher than 2 Hz appear after the arrival of seismic waves along different cable spans (c), from km 7.48 to 10.20.

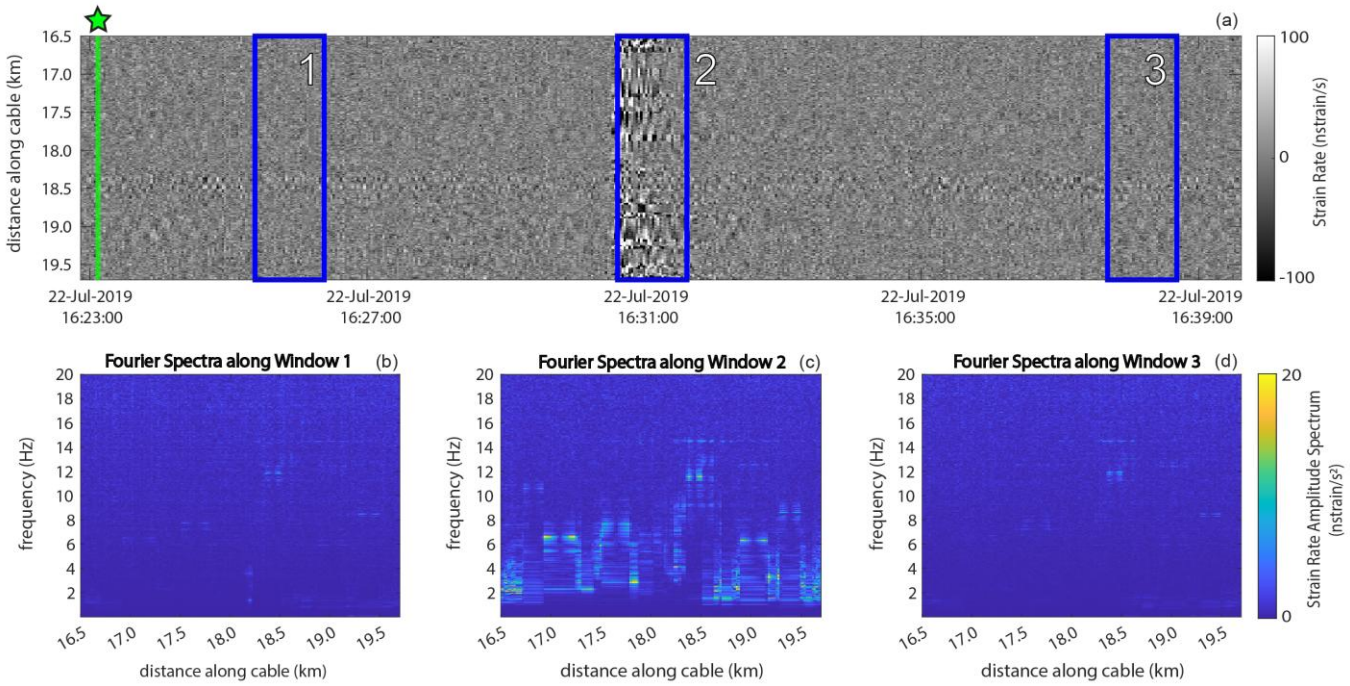

Supplementary Figure 2. High-frequency vibrations triggered along the MEUST fibre cable after a M_L-3.9 earthquake is recorded by DAS. (a) Low-pass filtered strain rate between km 16.50 and 19.70 along the MEUST cable, from 22-July-2019 16:23:00 to 16:39:00 UTC. Strain rate is filtered below 20 Hz. (green star) Origin time of the M_L-3.9 earthquake of Fig. 1 is indicated as reference. Waves trapped along certain cable sections can be observed in Window 2, after the arrival of seismic waves. (b), (c) and (d) Fourier Spectra between km 16.50 and 19.70 of a 1-min-long window starting: 2 min and 16 s after the earthquake (1), 7min and 29 s after the earthquake (2) and 14 min and 34 s after the earthquake (3), respectively. No significant signals are appreciated in Fourier spectra (b) and (d). Fundamental frequencies higher than 2 Hz appear after the arrival of seismic waves along different cable spans (c), from km 16.50 to 19.70.

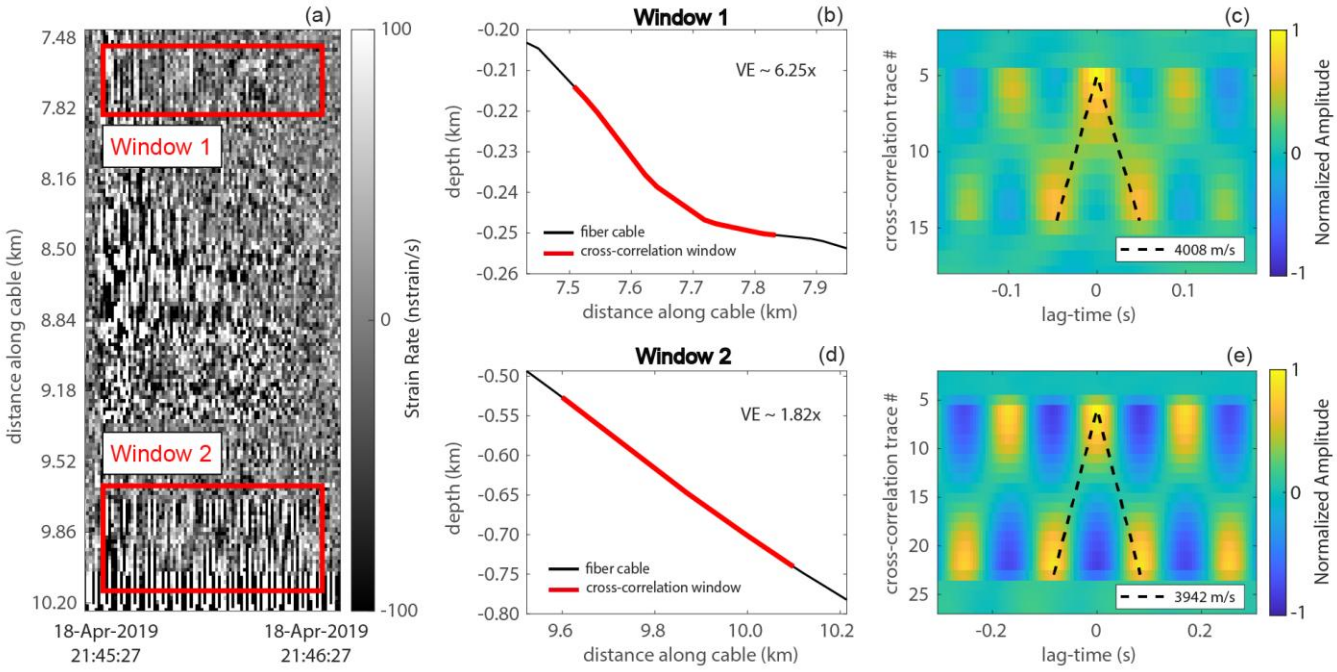

Supplementary Figure 3. Longitudinal trapped waves detected by DAS along cable segments of the HCMR cable featuring earthquake-triggered vibrations. (a) Low-pass filtered strain rate between km 7.48 and 10.20 along the HCMR cable, from 18-April-2019 21:45:27 to 21:46:27 UTC. Strain rate is filtered below 20 Hz. (red rectangles) Two 60-s-long windows of 172.80 (1) and 345.60 m (2) width are indicated as reference. (b) Bathymetry profile between km 7.45 and 7.95 along the cable path (VE stands for Vertical Exaggeration). The red line highlights the location of window 1 in (a). (c) Cross-correlation traces calculated over window 1 in (a), and relative to the trace reference number 5, km 7.60 along the cable. Amplitudes are normalized by the maximum of the cross-correlation traces. A longitudinal trapped wave bouncing forward and backward along the cable span with a speed of 4008 m/s can be clearly observed (black dashed lines). (d and e) Same as b, and c, but for a cable section traversing the continental slope between km 9.5 and 10.2, window 2 in (a).

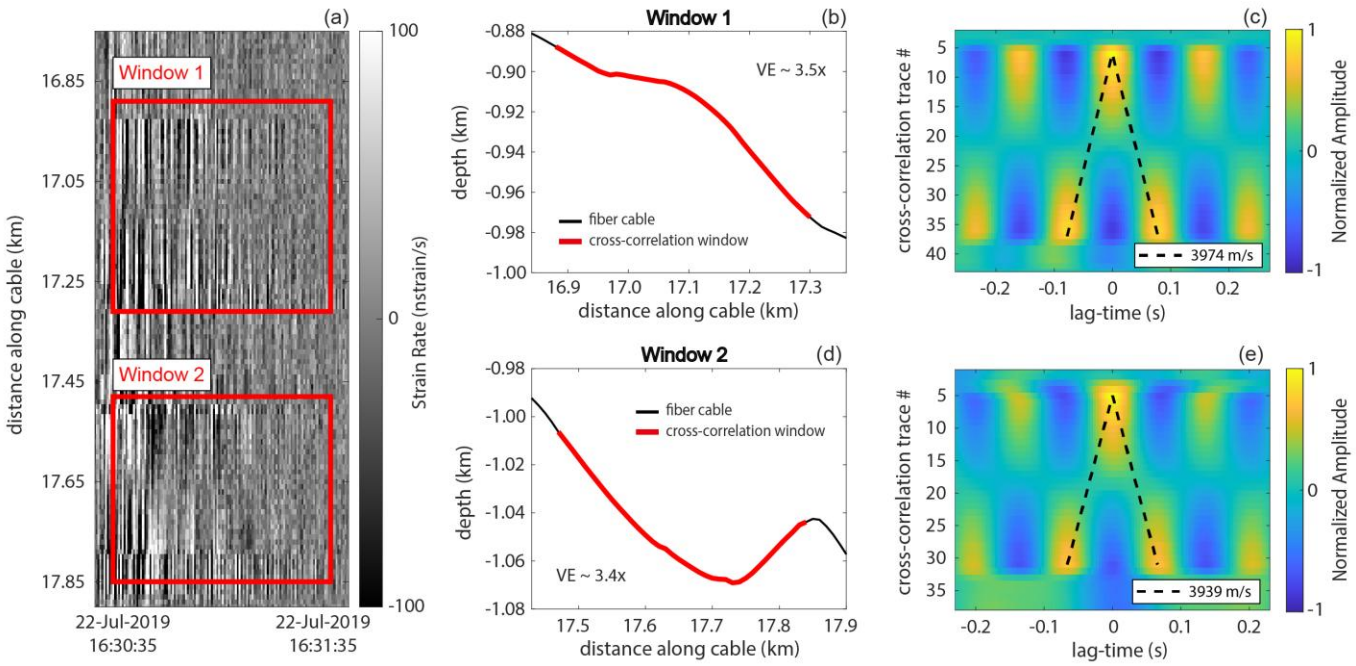

Supplementary Figure 4. Longitudinal trapped waves detected by DAS along cable segments of the MEUST cable featuring earthquake-triggered vibrations. (a) Low-pass filtered strain rate between km 16.75 and 17.90 along the MEUST cable, from 22-July-2019 16:30:35 to 16:31:35 UTC. Strain rate is filtered below 20 Hz. (red rectangles) Two 60-s-long windows of 420 (1) and 370 m (2) width are indicated as reference. (b) Bathymetry profile between km 16.84 and 17.36 along the cable path (VE stands for Vertical Exaggeration). The red line highlights the location of window 1 in (a). (c) Cross-correlation traces calculated over window 1 in (a), and relative to the trace reference number 5, km 16.94 along the cable. Amplitudes are normalized by the maximum of the cross-correlation traces. A longitudinal trapped wave bouncing forward and backward along the cable span with a speed of 3974 m/s can be clearly observed (black dashed lines). (d and e) Same as b, and c, but for a cable section presumably suspended between km 17.43 and 17.90, window 2 in (a).

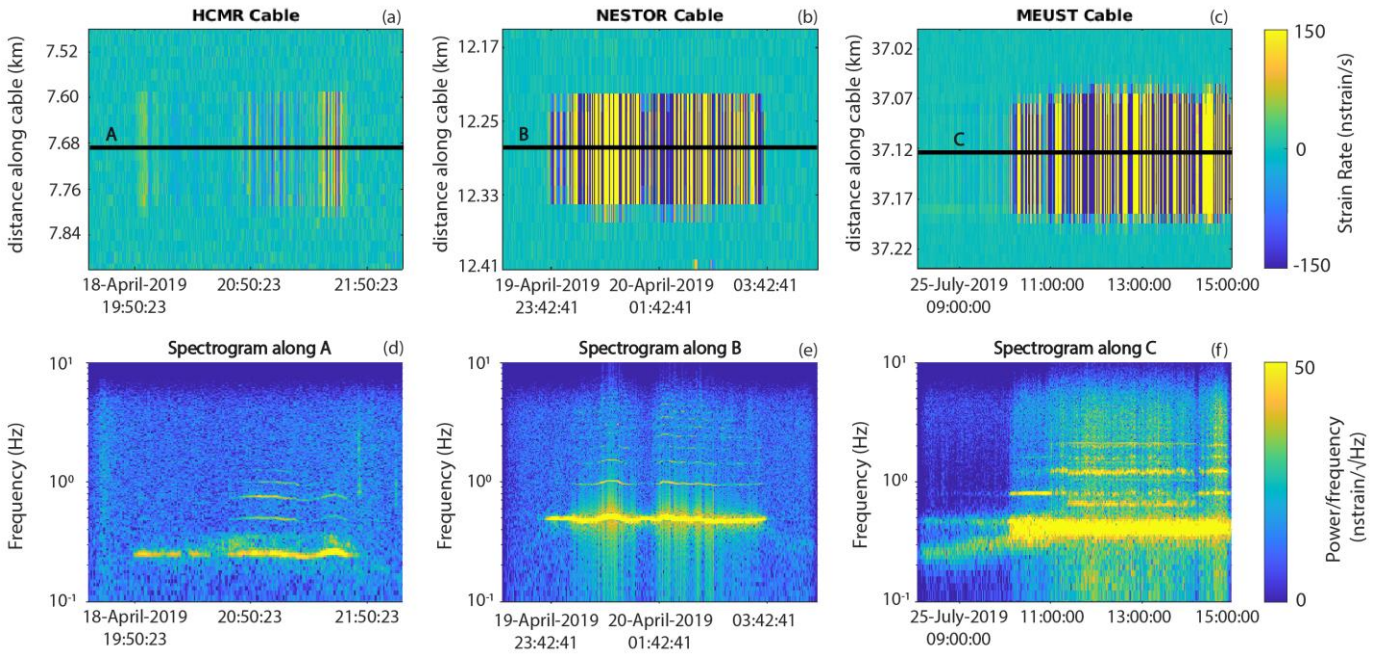

Supplementary Figure 5. Harmonics of Vortex-Induced Vibrations (VIV) recorded by DAS along suspended sections of submarine fibre cables. Low-pass filtered strain rate between km 7.52 and 7.84 from 18-April-2019 19:20:23 to 22:20:23 UTC along the HCMR cable (a), between km 12.17 and 12.41 from 19-April-2019 22:42:41 to 20-April 04:42:41 UTC along the NESTOR cable (b), and between km 37.02 and 37.22 from 25-July-2019 08:30:00 to 15:00:00 along the MEUST cable (c). DAS-strain rate data are filtered below 5 Hz. Black lines indicate the center of the cable segment featuring Low-Frequency (LF) oscillations. (d, e, f) Spectrograms of strain rate at A, B and C, respectively. Higher harmonic frequencies of VIV are excited along cable segments displaying LF oscillations.

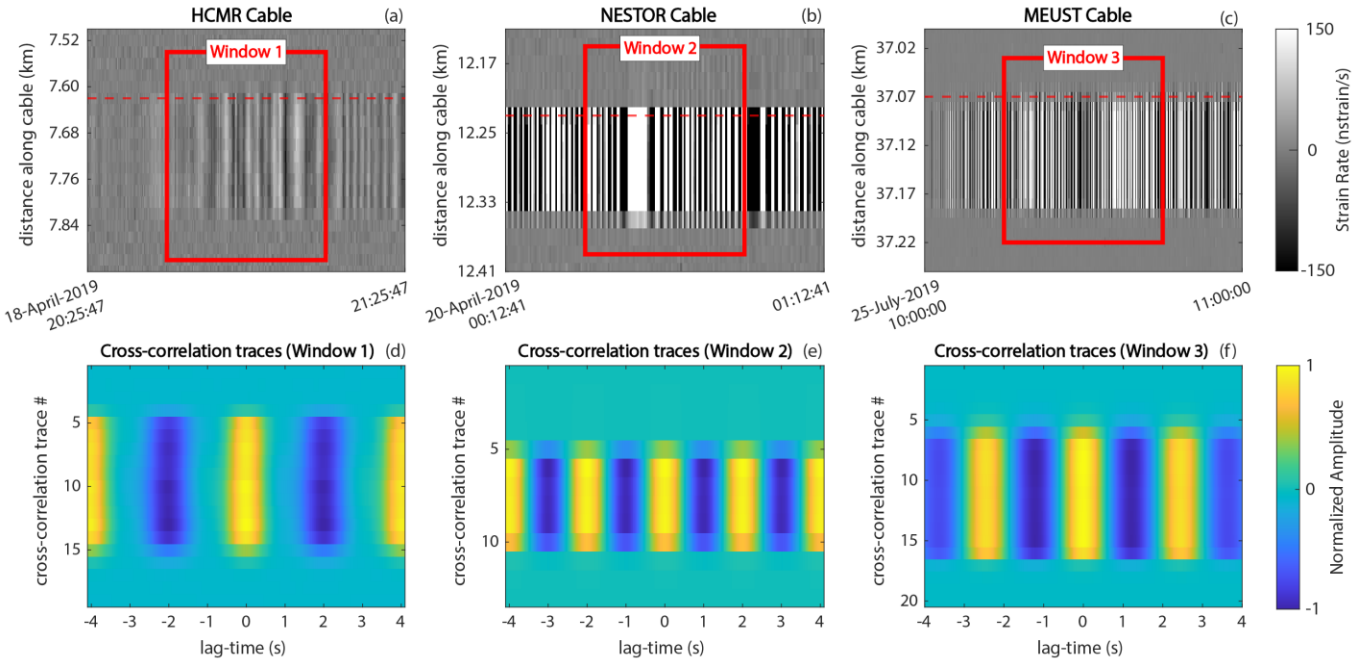

Supplementary Figure 6. Cross-correlation analysis of underwater fibre cables displaying Low-Frequency oscillations. Low-pass filtered strain rate between km 7.52 and 7.90 from 18-April-2019 20:25:47 to 21:25:47 UTC along the HCMR cable (a), between km 12.17 and 12.41 from 20-April-2019 00:12:41 to 01:12:41 UTC along the NESTOR cable (b), and between km 37.02 and 37.22 from 25-July-2019 10:00:00 to 11:00:00 along the MEUST cable (c). DAS-strain rate data are filtered below 2 Hz. (red rectangles) 30-min-long windows of strain rate of 345.60 (window 1), 230.40 (window 2) and 190 (window 3) m width for the HCMR, NESTOR and MEUST cable, respectively. (d, e and f) Cross-correlation traces calculated over window 1, 2 and 3 respectively. Dashed red lines in a, b and c indicate the reference traces used for cross-correlation. Amplitudes are normalized by the maximum of the cross-correlation traces. The cross-correlation of cable segments featuring Low-Frequency oscillations does not reveal cable waves.

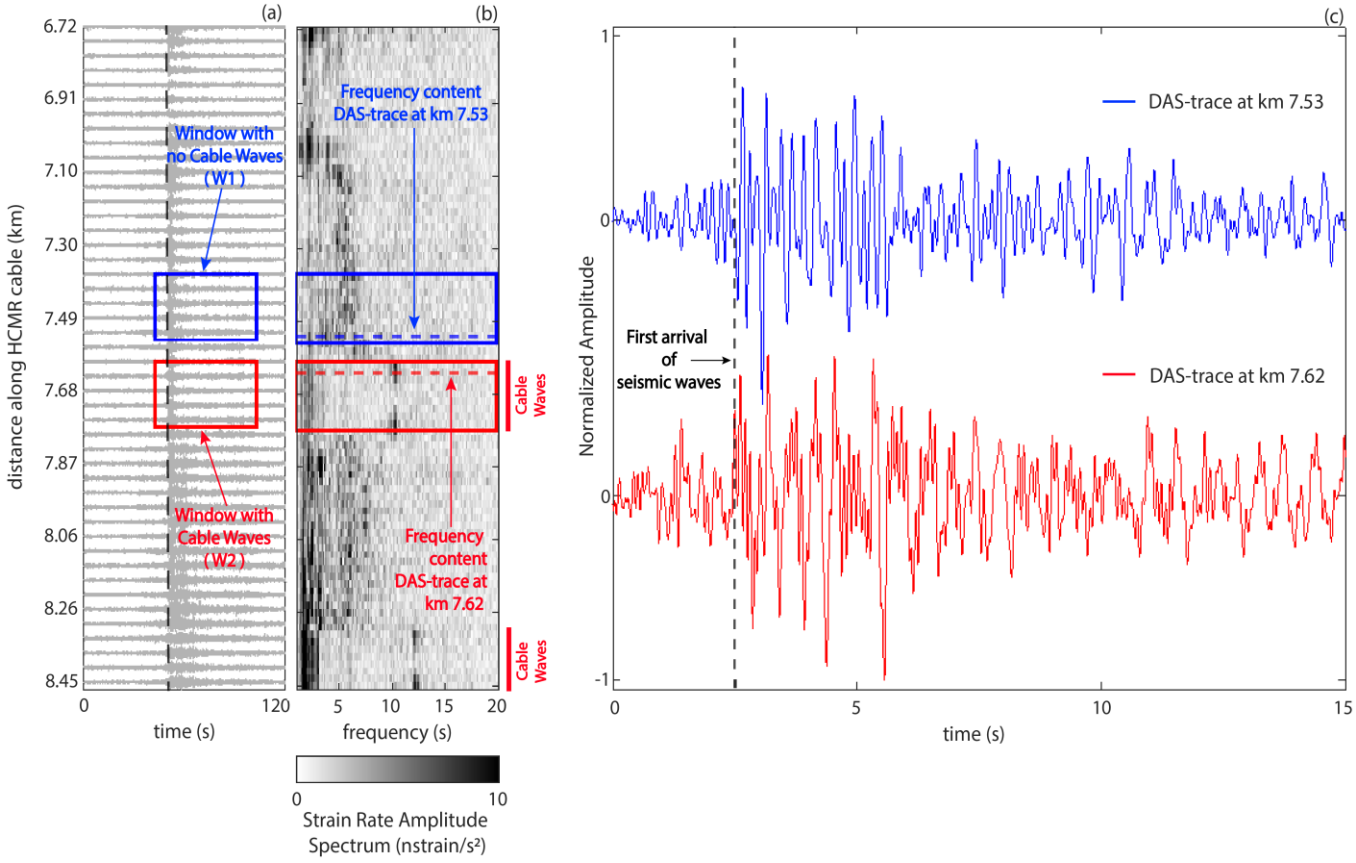

Supplementary Figure 7. Noise generated by cable waves in DAS-strain rate recordings of the HCMR cable. (a) 120-s-long traces of band-pass filtered strain rate between km 6.72 and 8.45 of the HCMR cable. Traces are filtered between 1 and 12 Hz and are represented each 38.4 m. (dashed line) Arrival of seismic waves due to the M_L-3.7 earthquake of Fig. 1. (blue and red rectangles) As reference, 60-s-long windows of 172.80 m width indicate whether cable waves are absent (W1) or detected (W2), respectively. (b) Fourier spectra between km 6.72 and 8.45 of a 60-s-long window starting at the same time of W1. (red and blue rectangles) Frequency content of W1 and W2, respectively. (c) 15-s-long traces of strain rate along: km 7.53 in W1 (blue), and km 7.62 in W2 (red). Amplitudes are normalized by the maximum strain rate of each channel. Cable waves are clearly recorded in W2, which may explain the high monochromatic noise that dominates the signal along the DAS-trace in km 7.62, after the arrival of seismic waves, compared to the DAS-trace in km 7.53.

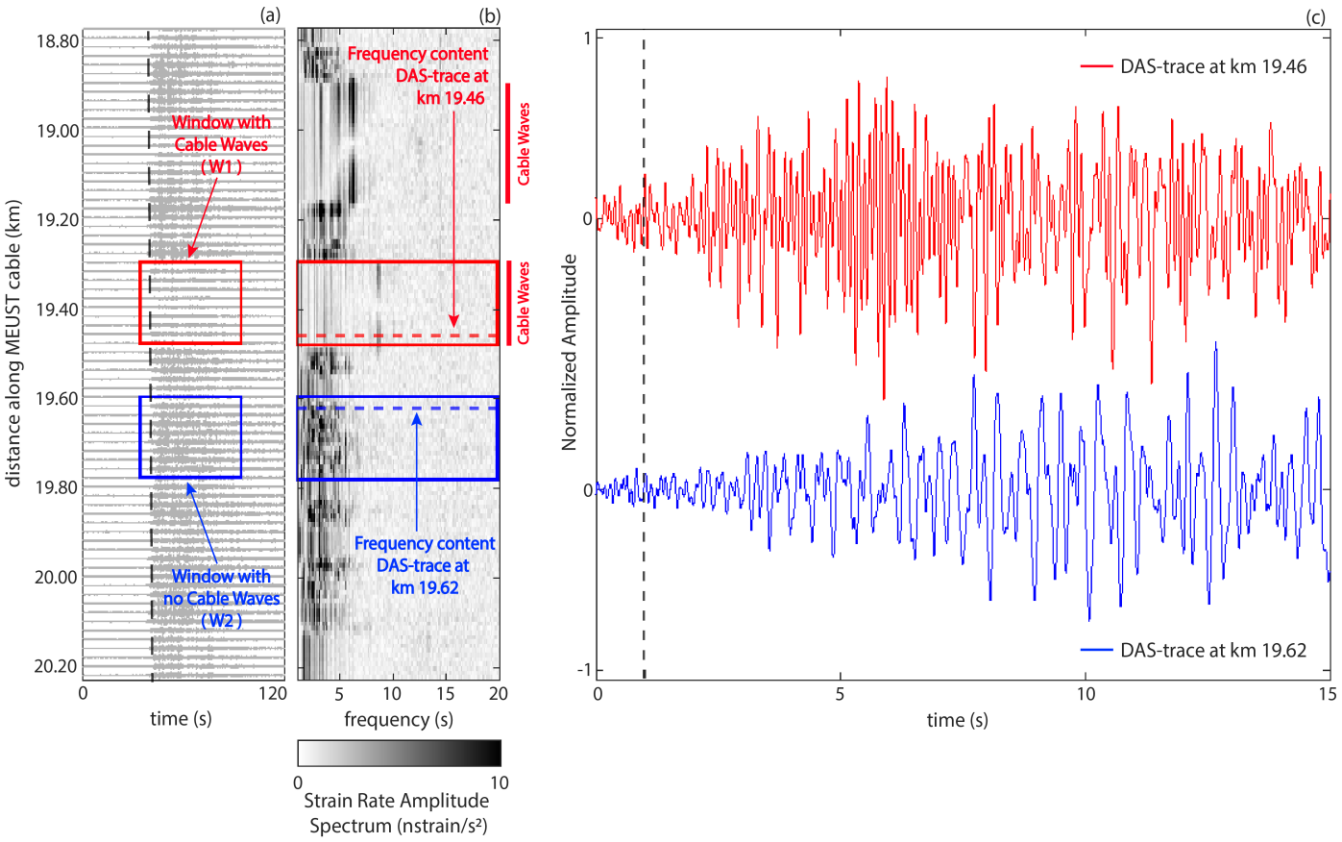

Supplementary Figure 8. Noise generated by cable waves in DAS-strain rate recordings of the MEUST cable. (a) 120-s-long traces of band-pass filtered strain rate between km 18.80 and 20.20 of the MEUST cable. Traces are filtered between 1 and 12 Hz and are represented each 20 m. (dashed line) Arrival of seismic waves due to the M_L-3.9 earthquake of Fig. 1. (red and blue rectangles) As reference, 60-s-long windows of 180 m width indicate whether cable waves are detected (W1) or absent (W2), respectively. (b) Fourier spectra between km 18.80 and 20.20 of a 60-s-long window starting at the same time of W1. (red and blue rectangles) Frequency content of W1 and W2, respectively. (c) 15-s-long traces of strain rate along: km 19.46 in W1 (red), and km 19.62 in W2 (blue). Amplitudes are normalized by the maximum strain rate of each channel. Cable waves are clearly recorded in W1, which may explain the high monochromatic noise that dominates the signal along the DAS-trace in km 19.46, after the arrival of seismic waves, compared to the DAS-trace in km 19.62.

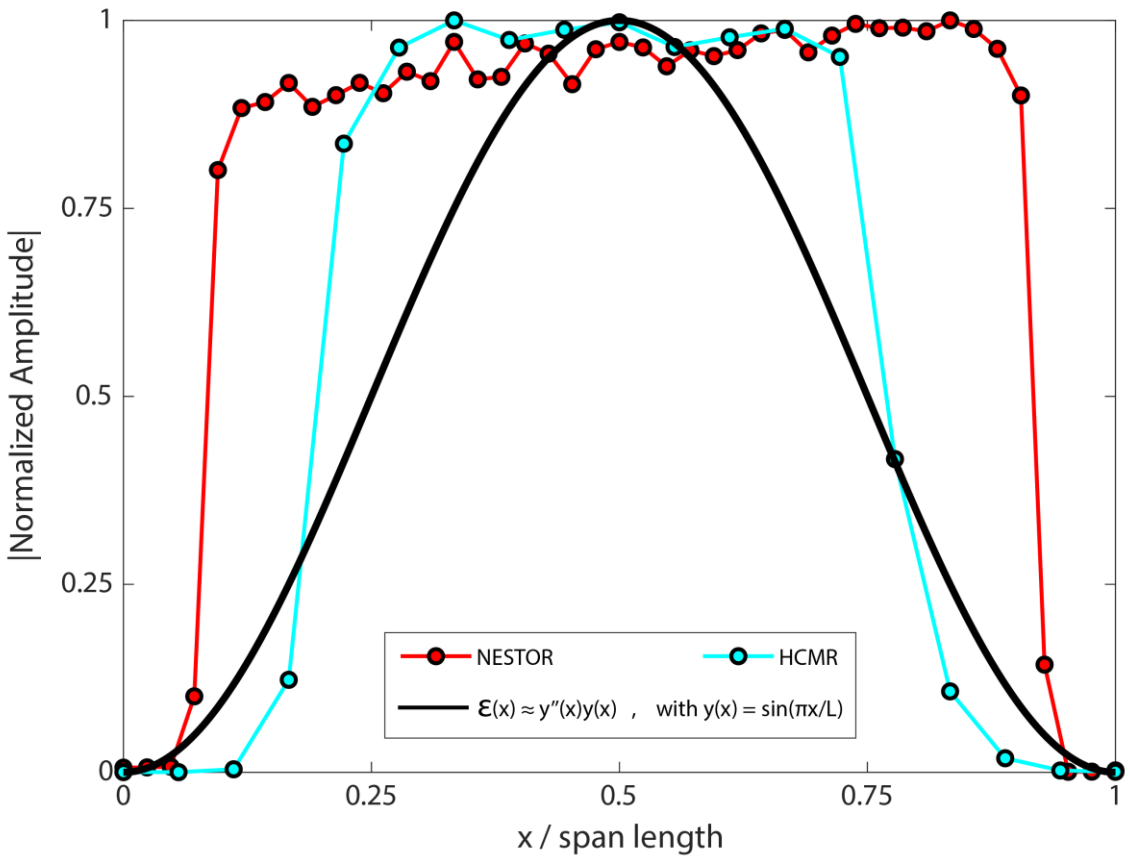

Supplementary Figure 9. Normal modes of Low-Frequency (LF) oscillations compared to longitudinal strain predicted by the beam theory. (red and cyan) Dominant normal modes of LF oscillations recorded by DAS along the NESTOR and HCMR cable, respectively. (black) Longitudinal strain ($\boldsymbol{\varepsilon}_{(x)}$) of a long and slender beam predicted by Timoshenko's beam theory as a function of the beam's deflection ($y_{(x)}$) and bending ($y''_{(x)}$). It is assumed that fibres have mode-shapes given by a sine function: $y_{(x)} = \sin(\pi x/L)$. Amplitudes in the vertical and horizontal axis are normalized by the maximum strain rate and the cable span length (L), respectively. The relation $\boldsymbol{\varepsilon}_{(x)} = y''_{(x)}\, y_{(x)}$ explains well the zero strain at both ends of the dominant normal modes, and the absence of strain nodes within the vibrating span. However, it predicts a maximum of strain at the mid-span, which is different from the quasi-uniform strain of the observed dominant normal modes.

Proper Orthogonal Decomposition based on DAS-recorded time series of strain rate.

According to Feeny (2002), Proper Orthogonal Decomposition (POD) is a statistical method that is used to find optimal distributions of energy from a set of time series. POD is commonly applied to a dataset of dynamical quantities recorded at *M* locations (Feeny, 2002). Here, *M* stands for the number of channels along the fibre cable that record DAS-strain rate (x) from a time t_1 to t_N, such as $x_i = (x_i(t_1), x_i(t_2), \ldots, x_i(t_N))^T$, for i = 1, 2, . . . , *M*. Prior to POD calculations, time series of DAS-strain rate are used to generate a *N* x *M* matrix, as follows (Feeny, 2002):

$$\mathbf{X} = [\, x_1, x_2, \ldots, x_M \,]$$

Then, a *M* x *M* correlation matrix $\mathbf{R} = (1/N)\mathbf{X}^T\mathbf{X}$ is formed, from which eigenvectors ($\mathbf{v}$) and eigenvalues ($\boldsymbol{\lambda}$) are extracted. The correlation matrix $\mathbf{R}$ is real and symmetric, which guarantees that $\mathbf{v}$ and $\boldsymbol{\lambda}$ are orthogonal (Feeny, 2002). Moreover, $\mathbf{v}$ contains the proper orthogonal modes (POMs) and $\boldsymbol{\lambda}$ the proper orthogonal values (POVs) of $\mathbf{R}$, respectively, i.e. the principal axes of inertia of the DAS-data and the signal power of each corresponding POM (Feeny and Kappagantu, 1998; Lumley, 1967; Cusumano and Bai, 1993; Cusumano et al., 1993; Berkooz et al., 1993).

POMs can be used as basis functions to decompose the dynamics of the DAS-recordings into modal co-ordinates $\mathbf{q}(t)$ (Han and Feeny, 2001). To do so, a proper orthogonal modal matrix $\mathbf{V}$ is defined, as follows (Feeny, 2002):

$$\mathbf{V} = [\, \mathbf{v}_1, \mathbf{v}_2, \ldots, \mathbf{v}_M]$$

Then, modal co-ordinates with elements $q_i(t)$, $i = 1, 2, \ldots, M$ are defined, such that (Feeny, 2002):

$$x(t) = \sum_{i=1}^{M} q_i(t)\mathbf{v}_i = \mathbf{Vq}$$

The proper orthogonal coordinates (POCs) time series $q_i(t)$ can be extracted from (Feeny, 2002):

$$\mathbf{Q} = \mathbf{XV}$$

where,

$$\mathbf{Q} = [\, q_1, q_2, \ldots, q_M \,]$$

Each modal co-ordinate represents the dynamics in the axis of a corresponding POM (Feeny, 2002).

References:

Feeny, B. F. (2002). On proper orthogonal co-ordinates as indicators of modal activity. *Journal of Sound and Vibration*, *255*(5), 805-817.

Feeny, B. F., & Kappagantu, R. (1998). On the physical interpretation of proper orthogonal modes in vibrations. *Journal of sound and vibration*, *211*(4), 607-616.

Lumley, J. L. (1967). The structure of inhomogeneous turbulent flows. *Atmospheric turbulence and radio wave propagation*, 166-178.

Cusumano, J. P., & Bai, B. Y. (1993). Period-infinity periodic motions, chaos, and spatial coherence in a 10 degree of freedom impact oscillator. *Chaos, Solitons & Fractals*, *3*(5), 515-535.

Cusumano, J. P., Sharkady, M. T & Kimble, B. W. (1993). Spatial coherence measurements of a chaotic flexible-beam impact oscillator. *Aerospace Structures: Nonlinear Dynamics and System Response, American Society of Mechanical Engineers* (33), 13-22.

Berkooz, G., Holmes, P., & Lumley, J. L. (1993). The proper orthogonal decomposition in the analysis of turbulent flows. *Annual review of fluid mechanics*, *25*(1), 539-575.

Han, S., & Feeny, B. F. (2001). Enhanced proper orthogonal decomposition for the modal analysis of homogeneous structures. *Journal of Vibration and Control*, *8*(1), 19-40.